

# How does salinity shape ocean circulation and ice geometry on Enceladus and other icy satellites?

Wanying Kang<sup>1\*</sup>, Tushar Mittal<sup>1</sup>, Suyash Bire<sup>1</sup>, Jean-Michel Campin<sup>1</sup>, and John Marshall<sup>1</sup>

<sup>1</sup>*Earth, Atmospheric and Planetary Science Department, Massachusetts Institute of Technology, Cambridge, MA 02139, USA*

Of profound astrobiological interest is that not only does Enceladus have a water ocean, but it also appears to be salty, important for its likely habitability. Here, we investigate how salinity affects ocean dynamics and equilibrium ice shell geometry and use knowledge of ice shell geometry and tidal heating rates to help constrain ocean salinity. We show that the vertical overturning circulation of the ocean, driven from above by melting and freezing and the temperature dependence of the freezing point of water on pressure, has opposing signs at very low and very high salinities. In both cases, heat and freshwater converges toward the equator, where the ice is thick, acting to homogenize thickness variations. In order to maintain observed ice thickness variations, ocean heat convergence should not overwhelm heat loss rates through the equatorial ice sheet. This can only happen when the ocean's salinity has intermediate values, order 20 psu. In this case polar-sinking driven by meridional temperature variations is largely canceled by equatorial-sinking circulation driven by salinity variations and a consistent ocean circulation, ice shell geometry and tidal heating rate can be achieved.

Since the Cassini and Galileo mission, Enceladus (a satellite of Saturn) and Europa (a satellite of Jupiter) have been revealed to have a high astrobiological potential, satisfying all three

necessary conditions for life: 1) the presence of liquid water <sup>1,2</sup>, 2) a source of energy <sup>3,4</sup>, and 3) a suitable mix of chemical elements <sup>1,5-10</sup>. In particular, the geyser-like sprays ejected out from the fissures over Enceladus's south pole <sup>11-13</sup> provide us a unique opportunity to understand the chemistry and dynamics of the Enceladus' interior without landing on and drilling through the 20-km ice shell. With the samples collected by Cassini near these geysers, CO<sub>2</sub>, methane <sup>5</sup>, sodium salt <sup>1</sup>, hydrogen <sup>7</sup>, and macromolecular organic compounds <sup>8</sup> have been found. These various compositions set Enceladus's chemical and biological environment <sup>9,10</sup> as well as the likelihood of an induced magnetic field and potential ocean dynamics due to electromagnetic coupling <sup>14</sup>. Furthermore, the ocean composition directly influences global-scale ocean dynamics. In particular, the Cassini observations illustrate that the ocean has some salts, likely due to water-rock interaction between Enceladus's ocean and rocky porous core <sup>15</sup>, leading to a consequent change in physical properties vis-à-vis fresh water oceans.

The ocean circulation on Enceladus is driven by the heat/salinity flux from both the silicate core at the bottom <sup>3</sup> and the ice shell at the top <sup>4,16,17</sup>. However, even if all these fluxes were known and prescribed, the circulation in a salty ocean would be completely different from that in a fresh ocean, because salinity controls whether density decreases or increases with temperature <sup>18</sup> (see Fig.1a) and thereby where sinking and rising occur (see Fig.1b). The heat transport by ocean circulation, in turn, shapes the ice shell geometry. Moreover, depending on the salinity, bottom heating released by hydrothermal vents may or may not increase the buoyancy of the water (due to the negative thermal expansion coefficient of fresh water close to its freezing temperature), and that in turn strongly affects the dynamics of hydrothermal vents.

Although there has been increasing focus on the ocean dynamics of Enceladus (and other icy moons) <sup>19,20</sup>, the role of salinity has not yet been systematically explored in a dynamical ocean model <sup>21</sup>. For Enceladus, observational inferences of salinity remain uncertain. The sodium-enriched samples taken from the south pole sprays by Cassini are found to have a salinity between 5 psu (g/kg) and 20 psu, and is considered as a lower bound on ocean salinity, given that the interaction with the environmental cold water vapor is likely to draw down the salinity of salty droplets in the sprays <sup>1</sup>. Using the size of silica nano-particles carried along in the sprays, an upper bound on salinity is perhaps 40 psu, depending on the pH and the dynamics of hydrothermal vents <sup>6</sup>. Another salinity estimate comes from the requirement to keep the geysers' liquid-gas interface convectively active and thus resilient to freezing. For a scenario without gas bubbles <sup>22</sup>, ocean salinity is suggested to be at least 17 psu <sup>23</sup>. Since these estimates are based on products from the eruptive plumes of Enceladus, there are potentially additional uncertainties related to jet formation and how representative they are of the overall ocean, especially if the source region of the former are strongly influenced by hydrothermal plumes <sup>3,15</sup>. Finally, calculations of thermochemical equilibria over a range of hydrothermal and freezing conditions for chondritic compositions (with a water-rock ratio  $\sim 1$ ) suggest that ocean salinity is in the range 2-20 psu (most likely  $< 10$  psu) <sup>15,24,25</sup>. Since Enceladus's core is still geochemically active, the actual water-to-rock ratio is likely higher for Enceladus's ocean, thus leading to a lower present-day ocean salinity, even after accounting for freezing of a fresh 21 km thick ice shell.

In this study, we explore how ocean circulation and its ability to deliver heat to the ice shell changes as the mean salinity of the ocean is changed. This can provide further constraints on the

salinity of Enceladus's ocean in the light of its relatively well constrained ice shell geometry <sup>26–30</sup>, and inform inferences about Europa's ice shell geometry if its salinity were known <sup>31</sup>. In addition, a better understanding of the dynamics of a salty ocean is critical for inferring habitability from the compositions of geyser ejecta <sup>6</sup> and to understand the time-scales over which heat as well as potential hydrothermal and biosignatures are transported across the ocean (e.g., aggregation rate of silica particles formed at depth <sup>6</sup>).

To achieve this goal, we configure the Massachusetts Institute of Technology ocean model (MITgcm <sup>32,33</sup>) to simulate Enceladus' ocean over a range of assumed mean salinities (4, 7, 10, 15, 20, 25, 30, 35 and 40 psu). The ocean is imagined to be encased by an ice shell whose thickness varies meridionally (solid curve in Fig.1b) and forced by the freezing/melting rate which is demanded to maintain a poleward-thinning ice geometry <sup>30</sup> (dashed curve in Fig.1b, see methods for details) in the face of ice flow which smooths it out <sup>34–36</sup>. By so doing, we guarantee that the freezing rate and hence the salinity flux at the water-ice interface are plausible; meanwhile, we prevent the ice shell from changing in response to the ocean heat transport. This is equivalent to assuming that the tidal heating generated in the ice shell can accommodate the heat needed to maintain the prescribed freezing/melting rate. The degree to which the heat budget is in balance informs us of the plausibility of the assumed salinity as follows. We diagnose the water-ice heat exchange from the model, and infer the tidal dissipation rate in the ice shell required to close the heat budget, i.e., the sum of latent heating, tidal dissipation and heat input from the ocean which balances the heat loss to space by heat conduction through the ice. This inferred tidal dissipation rate can then be compared against that given by an ice shell tidal dissipation model. More technical

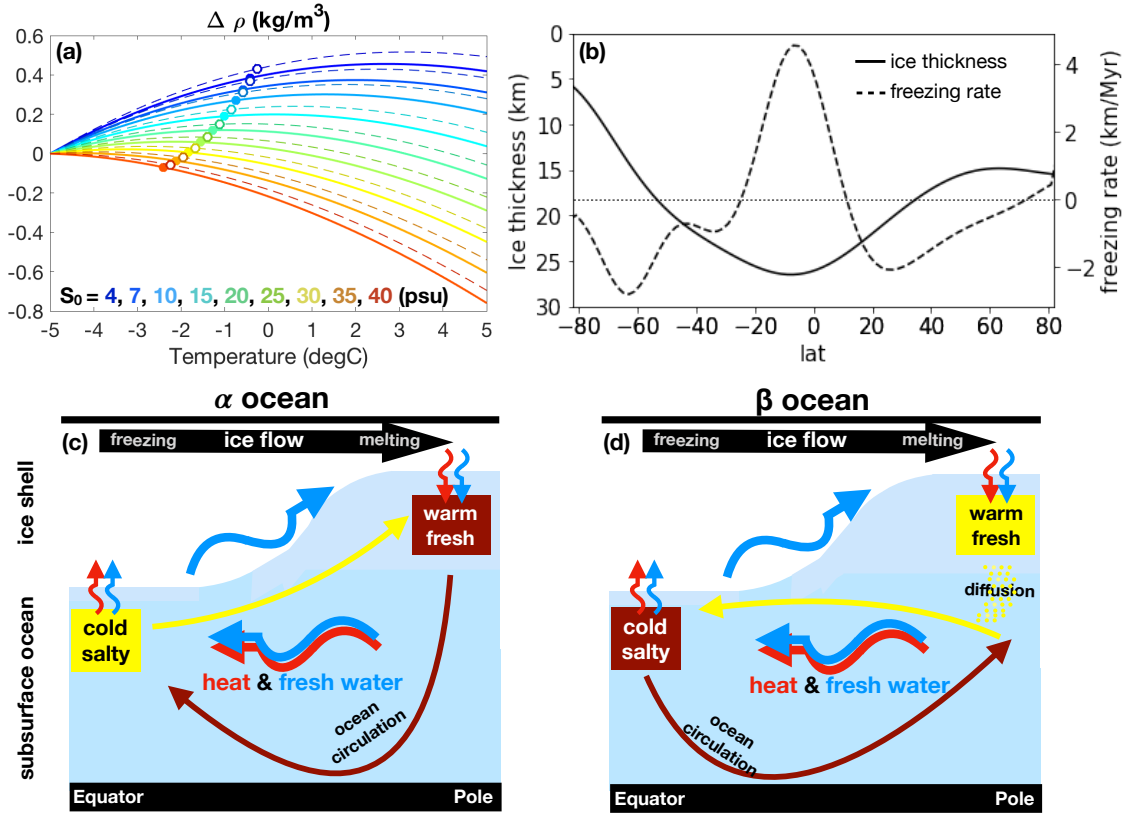


Figure 1: (a) The density anomaly of water near the freezing point as a function of temperature for various salinities and two pressures. From cold to warm colors denotes increasing salinity (see color-coded legend). Pressure underneath thick ice at the equator is used to compute the solid curves and pressure underneath the south polar ice shell is used for the dashed curves. The density at  $-5^{\circ}\text{C}$  for each case is chosen as the reference point. (b) Ice shell thickness of Enceladus (solid curve, left y-axis). The freezing rate (positive) and melting rate (negative) is plotted required to maintain a steady state implied by an ice-flow model (dashed curve, right y-axis). Schematics of circulation and associated transport of heat (red wiggly arrows) and freshwater (blue wiggly arrows) for (c) the alpha ocean in which temperature dominates density variations with sinking at the poles and (d) the beta ocean in which salinity dominates with sinking at the equator. The dark brown arrows denote sinking of dense water, light yellow arrows denote rising of buoyant water. The circulations are forced by the freezing/melting required to counterbalance the down-gradient ice flow (thick black arrows marked at the top) and by variations in the freezing point of water due to pressure.

details are given in the method section.

The observed poleward-thinning of the ice shell <sup>26–30</sup> (solid curve in Fig.1b) has two important consequences, as sketched in Fig.1(c,d). First, the relatively thick ice near the equator creates high pressure and depresses the freezing point and hence the ocean is cold there. This can be seen from the rightward shift of open circles (freezing point at the base of the south polar ice shell) relative to the filled circles (freezing point at the base of the equatorial ice shell) in Fig.1a. Secondly, to sustain the thickness variation from being smoothed out by the down-gradient ice flow acting over geological time-scales <sup>34–36</sup> (black arrows in Fig.1c,d), the equatorial ice must freeze over time (dashed curve in Fig.1b) increasing the local salinity. The opposite occurs in polar regions where ice is melting. Therefore, just beneath the ice, water in low latitudes is colder and saltier than that near the poles, regardless of the mean salinity of the ocean (see the top two rows in Fig.2, also sketched in Fig.1c,d).

This pole-to-equator temperature and salinity contrast leads to variations in density which drive ocean circulation, as illustrated in the detailed solutions from our ocean model presented in Fig. 2. However, the relative contribution of temperature versus salinity to density depends on the mean salinity  $S_0$ . When  $S_0$  is greater than 22 psu, water expands with increasing temperature (see reddish curves in Fig.1a). A combination of low temperature and high salinity makes water denser under the thick equatorial ice shell relative to the poles, as shown in Fig.2-c3 and sketched in Fig.1d using dark brown color. Equatorial water therefore sinks, as shown in Fig.2-e3 (sketched in Fig.1d using a dark brown arrow). However, when  $S_0$  is below 22 psu, the thermal expansion coefficient

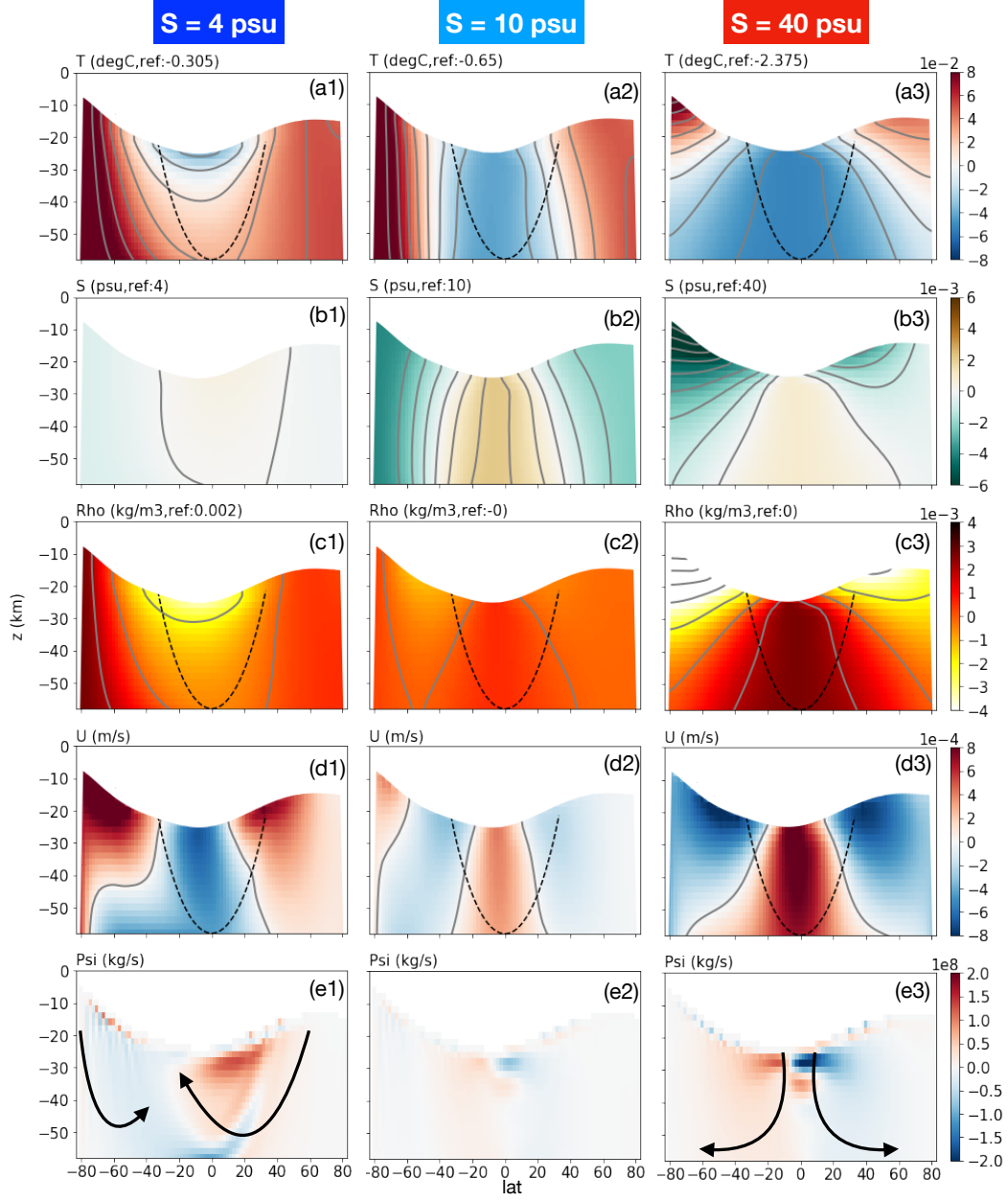


Figure 2: Ocean circulation and thermodynamic state for experiments driven by the glacial melt distributions shown in Fig. 1b for oceans with various mean salinities. From top to bottom shows temperature  $T$ , salinity  $S$ , density anomaly  $\Delta\rho$ , zonal flow speed  $U$  and meridional streamfunction  $\Psi$ . The left column presents results for a low salinity ocean ( $S_0 = 4$  psu), the right column for high salinity ( $S_0 = 40$  psu), and the middle column for an ocean with intermediate salinity ( $S_0 = 10$  psu). The reference temperature and salinity (marked at the top of each plot) are subtracted from  $T$  and  $S$  to better capture spatial patterns. Positive  $U$  indicates flow to the east and positive  $\Psi$  indicates a clockwise overturning circulation.

changes sign (see bluish curves in Fig.1a). This so-called anomalous expansion effect makes the temperature-induced density difference and the salinity-induced density difference partially cancel with one another. If salinity plays the more dominant role in determining density (this limit is known as the  $\beta$  ocean), the overturning circulation becomes one of sinking at the equator, as shown in Fig.2-e2 and sketched in Fig.1c using a dark brown arrow. But if temperature dominates instead (corresponding to a fresh,  $\alpha$  ocean), the overturning circulation flips direction with sinking over the poles because water is denser there (Fig.2-c1). This can be seen in Fig.2-e1, and the schematic in Fig.1c).

To present the transition from polar to equatorial sinking graphically, Fig.3 presents, for all nine experiments, the temperature induced density anomaly ( $-\alpha_T \Delta T$ ) and salinity induced density anomaly ( $\beta_S \Delta S$ ) at the equator, taking the water-ice interface at the north pole as the reference point (Fig.3 filled dots). Note that both  $\Delta S$  and  $-\Delta T$  are positive (the equator is always saltier and colder than the pole), the sign of the coordinates reflect the sign of  $\alpha_T$  and  $\beta_S$ :  $\beta_S$  is always positive, but  $\alpha_T$  increases from negative to positive as  $S_0$  increases. In the high  $S_0$  experiments,  $-\alpha_T \Delta T$  and  $\beta_S \Delta S$  have the same sign (upper right quadrant). In the low  $S_0$  experiments,  $-\alpha_T \Delta T$  and  $\beta_S \Delta S$  have opposite signs (lower left quadrant). The 45 degree tilted line denotes perfect cancellation. It passes between 7 psu and 10 psu, explaining why these two experiments have the weakest circulation amongst all others (the size of the circles are proportional to  $\Psi$ ).

Downwelling regions (low latitudes for  $S_0 = 10, 40$  psu and high latitudes for  $S_0 = 4$  psu) carry density, temperature and salinity anomalies, set at the ocean-ice interface, in to the interior



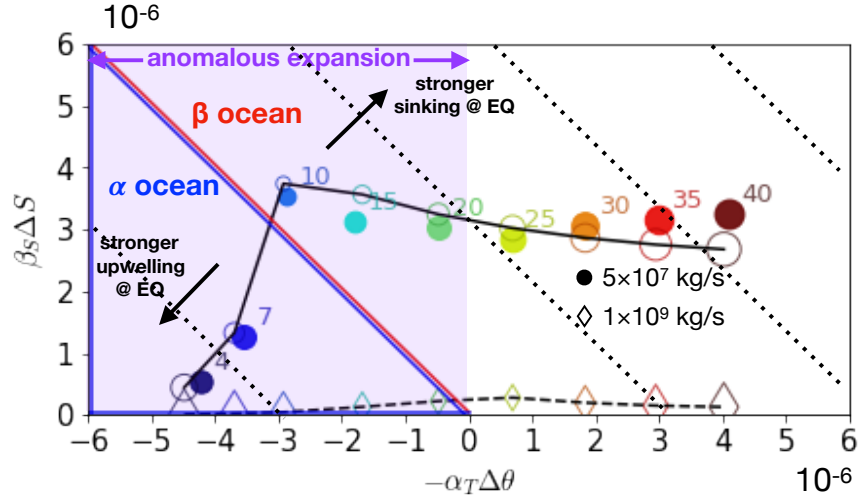


Figure 3: Regime diagram showing the influence of temperature and salinity anomalies on density as a function of mean salinity, and how the ocean's overturning circulation responds. Horizontal and vertical axes are the temperature and salinity induced density anomalies at the equator, relative to the north pole. Red (blue) solid lines encompass the  $\beta$  ocean ( $\alpha$  ocean) regime, in which the density is dominated by salinity (temperature) anomalies. Purple shading highlights the regime where anomalous expansion is present. The position of all our experiments in this space is represented by the symbols. The number on the shoulder of each dot gives the  $S_0$  used in that experiment. The size of each dot represents the amplitude of overturning circulation (the peak  $\Psi$  occurs in the northern hemisphere). As illustrated by the black arrows, circulation strengthens moving away from the transition line between  $\alpha$  ocean and  $\beta$  ocean. The empty dots connected by a black solid curve show the fit by a conceptual model (see text for details). Empty diamonds connected by a black dashed curve show a prediction made by the conceptual model assuming a more vigorous overturning circulation.

ocean. Note the bending of the temperature and salinity contours equatorward (poleward) when downwelling occurs at the poles (equator), as shown in Fig. 2. This results in meridional density gradients which are in a (generalised<sup>1</sup>) thermal wind balance with zonal currents (the “d” row in Fig. 2). Downwelling regions (low latitudes for  $S_0 = 10, 40$  psu and high latitudes for  $S_0 = 4$  psu) have predominantly eastward flow, with westward flow in upwelling regions. When the overturning circulation is weak ( $S_0 = 10$  psu), meridional density gradients are weak and the zonal flow is slow. In this case the temperature and salinity contours are mostly vertical (see the second column of Fig. 2).

Of particular interest is the meridional heat transport whose convergence results in ocean-ice heat exchange. It is shown in Fig. 4a for our nine experiments;  $S_0$  increases from bluish colors to reddish colors. As illustrated in Fig.1(c,d), irrespective of the sign of the overturning circulation, heat is always converged to the relatively cold low latitudes tending to melt the relatively thick ice shell there. This is a manifestation of the ice pump mechanism<sup>37</sup> which is driven by the dependence of the freezing point of water on pressure. The amplitude of the meridional heat flux varies by more than an order of magnitude being large (small) where the overturning circulation is strong (weak). This is readily understood because the heat flux is proportional to the product of the overturning strength multiplied by a temperature contrast – see *Czaja & Marshall 2006*<sup>38</sup>. The latter is broadly the same in all experiments but the former strongly depends on the mean salinity<sup>2</sup>.

---

<sup>1</sup>The terms associated with the horizontal component of Coriolis force must be included.

<sup>2</sup>The coldest and warmest locations are adjacent to the water-ice interface whose temperature is set by the local freezing point of water, whose meridional variation is dominated by pressure effects which are the same in all experiments. See Eq.9 for the dependence of freezing point on salinity and pressure.

Another aspect of interest is that in all experiments, heat is transported across the equator in to the southern hemisphere where the ice is thinner than in the northern hemisphere. This hemispheric asymmetry of meridional heat transport may be because the thickest ice shell and the strongest freezing occurs around 10°S instead of the equator (see Fig.1b). The amplitude ranges from a few to a dozen GW or so, depending on the strength of the overturning circulation. This can thus be a significant fraction of the 35GW of heating being generated by the tide. This further enhances the hemispheric asymmetry in ice thickness, providing another mechanism to induce hemispheric symmetry breaking of the ice thickness besides the ice-rheology feedback proposed by *Kang & Flierl 2020*<sup>39</sup>.

Given the meridional heat transport, we can infer the amount of tidal heating implied, assuming that the heat budget of the ice shell is in balance. Since the bottom of the ice is much warmer than its top, Enceladus loses around 50 mW/m<sup>2</sup> of heat to space in the global average, according to a 1D heat conduction model (Eq.10). At equilibrium, this heat loss ( $\mathcal{H}_{\text{cond}}$ ) must be in balance with the tidal heating generated in the ice shell  $\mathcal{H}_{\text{tide}}$ , the heat transmitted from the ocean to the ice  $\mathcal{H}_{\text{ocn}}$  and the latent heat release induced by freezing  $\rho_i L_f q$  (where  $\rho_i$  is the ice density,  $L_f$  is the fusion energy of water and  $q$  is the freezing rate shown in Fig.1b) thus:

$$\mathcal{H}_{\text{cond}} = \mathcal{H}_{\text{tide}} + \mathcal{H}_{\text{ocn}} + \rho_i L_f q \quad (1)$$

Knowing both  $\mathcal{H}_{\text{cond}}$  and  $\rho_i L_f q$ , and diagnosing  $\mathcal{H}_{\text{ocn}}$  from our ocean model<sup>3</sup> we can use the above

---

<sup>3</sup>We calculated  $\mathcal{H}_{\text{ocn}}$  in two ways. First, we directly diagnosed the heat exchange between ice and ocean. Secondly we calculate the meridional heat convergence (Fig.4a) and added the bottom heat flux (Eq.11) to it. They yield identical results, indicating that the ocean has reached equilibrium.

formula to infer  $\mathcal{H}_{\text{tide}}$ .

This inferred  $\mathcal{H}_{\text{tide}}$  from our suite of ocean solutions is shown by solid curves in Fig.4b. This should be compared to the tidal heating given from our tidal dissipation model plotted in the black dashed curves (details in the Methods section). Those ocean solutions with a strong overturning circulation converge a large amount of heat to low latitudes by advecting warm water equatorwards, which cannot be lost by conduction. The very fresh ocean with  $S_0 = 4$  psu yields the worst match between implied and predicted  $\mathcal{H}_{\text{tide}}$ . The discrepancy can be greater than  $100 \text{ mW/m}^2$  at some latitudes, twice as much as the global mean heat loss rate by heat conduction. Moreover, in this case, in order to maintain a balanced heat budget, the implied tidal heating generated in the ice shell needs to be significantly negative in equatorial regions!

To quantify the mismatch, we use the norm-1 of the difference between the inferred  $\mathcal{H}_{\text{tide}}$  and the predicted  $\mathcal{H}_{\text{tide}}$ , as shown in Fig. 4(c). It reaches a minimum when  $S_0$  is around 10 psu. The meridional heat transport and inferred  $\mathcal{H}_{\text{tide}}$  for  $S_0 = 10$  psu is shown by a thicker blue curve in Fig. 4(a,b). Because the temperature-induced density anomaly and salinity-induced density anomaly almost cancel one-another at this salinity (see Fig.3), the overturning circulation is weak (Fig.2-e2). As a result, less heat is converged equatorward (Fig.4b), and the inferred  $\mathcal{H}_{\text{tide}}$  no longer has negative values near the equator. In fact, the  $\mathcal{H}_{\text{tide}}$  given by the tidal dissipation model can roughly keep the ocean-ice system in balance when  $S_0$  is around 10 psu.

It is notable that the increase in the mismatch is much faster on the fresh side of 10 psu than the salty side (Fig.4c). This has its origin in the change of circulation pattern (in addition to the

reversal of the sense of overturning) as the ocean switches from  $\alpha$ - to  $\beta$ -control. As shown in Fig.2-e1, the overturning circulation in an  $\alpha$  ocean can directly connect the water-ice interface at the pole to equatorial regions; in contrast in a  $\beta$  ocean (Fig.2-e3), the circulation weakens moving poleward and almost completely vanishes in the fresh water lens formed under the polar ice shell. Such differences can be understood using Sandstrom's theorem <sup>40</sup>. In an  $\alpha$  ocean, the buoyancy gain at the equator is deeper down than the buoyancy loss at the poles and ocean circulation can always be energized against friction as polar dense water higher up the water column is transported to depth – see Fig.1c). However, in a  $\beta$  ocean, the reverse is true and equatorial dense water cannot easily be drawn upward to the polar ice shell without extra energy input by diffusion <sup>41</sup>. Strong stratification develops in the diffusive layer (Fig.2-c3), sustaining an upward buoyancy flux and keeping the water close to rest. This is indicated on the schematic diagram Fig.1d).

Thus far, we have been assuming that the heat required to balance conductive heat loss through the ice shell to space originates in the ice shell itself (the shell-heating scenario), motivated by our recent study <sup>20</sup>. However, the circulation pattern, the temperature/salinity profile, and the meridional heat transport are broadly similar (not shown), even if the heat is generated in the core. This is because the heating-induced bottom-to-top temperature difference is at most a few tens of milliKelvin, much smaller than the equator-to-pole temperature difference induced by the freezing point variations (Fig.2) which is order 0.1 Kelvin. In Fig. 4(d-f) we show the meridional heat transport, inferred tidal dissipation and mismatch index for the core-heating scenario. The best-matching salinity shifts to 15-20 psu, in broad agreement with the shell-heating scenario. However, the matching is less good overall, especially near the south pole. With no heat produced

in the ice shell (black dashed curved in panel e), the ice shell there will freeze over time, as heat is transported away by ocean circulation.

In summary, the numerical solutions presented above suggest that if Enceladus' ocean is of intermediate salinity, near the transition between an  $\alpha$  ocean and a  $\beta$  ocean, then equatorial convergence of heat is minimized, allowing a thick equatorial ice shell to be maintained. This is much less likely in very fresh or very salty oceans. Here, we build a conceptual model to highlight the key mechanism and explore a wider range of parameter space that can be applied to other icy moons.

We take the north pole as a reference and use the density anomaly at the equator  $\Delta\rho$  to represent the overall density contrast in the ocean. The temperature-related density anomaly is  $-\alpha_T\Delta\theta$ , and that due to salinity is  $\beta_S\Delta S$ , where  $\Delta\theta$  and  $\Delta S$  are the potential temperature and salinity anomaly at the equator relative to the north pole. We expect the overturning circulation to increase with the absolute value of  $\Delta\rho$ . For simplicity, we assume a linear form

$$\Psi = A \max(|-\alpha_T\Delta T + \beta_S\Delta S|, C), \quad (2)$$

where the constant  $A$  maps the density contrast on to the vigor of the overturning circulation. We introduce a term  $C = 1 \times 10^{-6}$  in Eq.2 which ensures that there is a finite but small circulation even if  $-\alpha_T\Delta\theta$  and  $\beta_S\Delta S$  perfectly cancel. We should note that  $\beta_S \approx 8 \times 10^{-4}/\text{psu}$  for all  $S_0$ , but  $\alpha_T$  depends sensitively on  $S_0$ , as given by the Gibbs Seawater Toolbox<sup>18</sup>.

The temperature contrast  $\Delta T$  is determined by the pressure-induced freezing point shift from

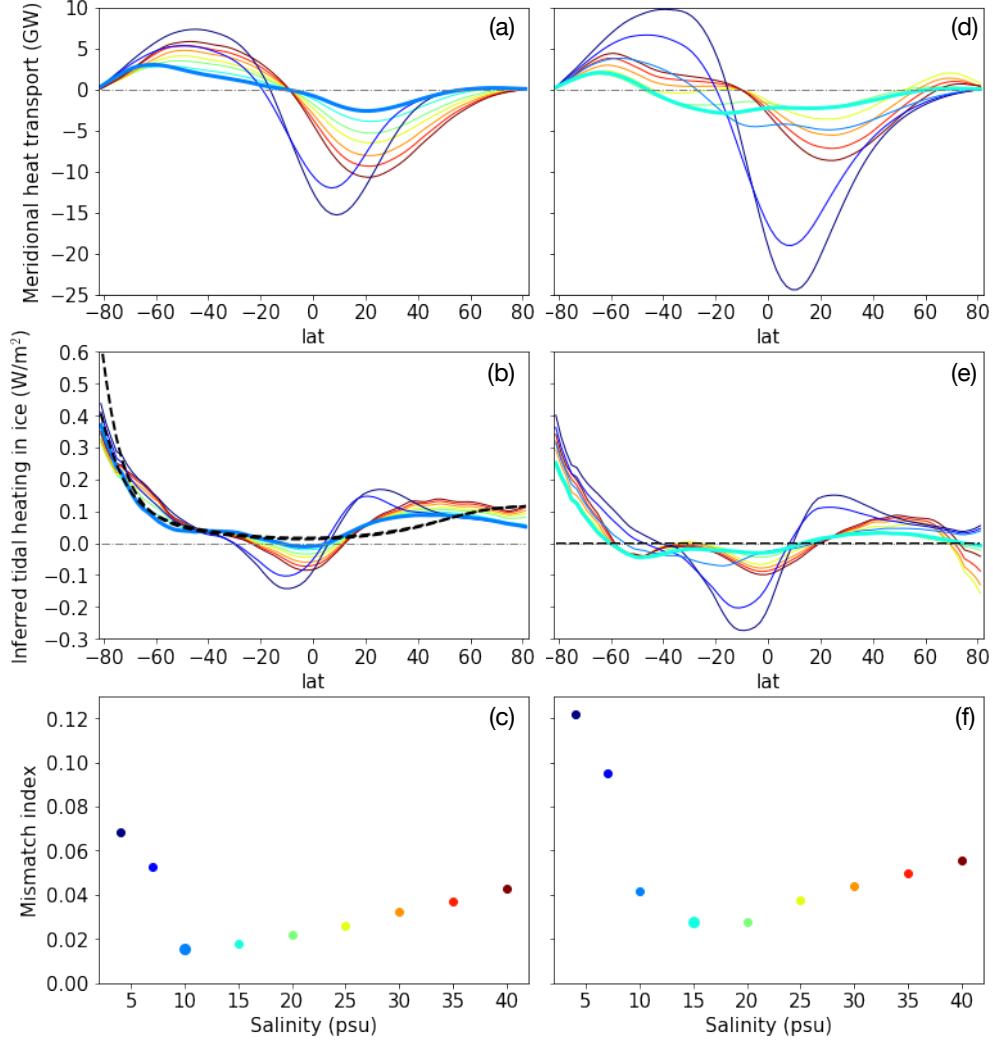


Figure 4: Meridional heat transport and inferred tidal heat rates as a function of assumed mean salinity.

The left column shows results from our ocean model assuming all the tidal heating occurs in the ice shell, and on the right from simulations in which all heating is in the core. Panel (a,b) show the meridional ocean heat transport and the inferred tidal heating generation in the ice sheet for experiments with various mean salinities  $S_0$ . The black dashed curve in panel (b) shows the profile of  $\mathcal{H}_{\text{tide}}$  predicted by a model of tidal heating in the ice shell. Panel (c) shows mismatch indices, defined by the norm-1 of the deviation of the inferred  $\mathcal{H}_{\text{tide}}$  from the predicted  $\mathcal{H}_{\text{tide}}$ , for various  $S_0$ . In all plots, on moving from cold to warm colors  $S_0$  increases from 4 psu to 40 psu. The exact  $S_0$  for each color can be read from the x-axis of panel (c). The right column presents the same information but for 15 simulations of our ocean model for core heating scenarios in which tidal heating in the ice shell  $\mathcal{H}_{\text{tide}}$  is assumed to be zero. The experiments with the best match salinity are highlighted by thicker curves and larger markers in all panels.

the north pole to the equator<sup>4</sup>,

$$\Delta T = b_0 \Delta P = b_0 \rho_i g \Delta H, \quad (3)$$

where  $b_0 = -7.61 \times 10^{-4}$  K/dbar,  $\rho_i = 917$  kg/m<sup>3</sup> is the ice density,  $g = 0.113$  m/s<sup>2</sup> is the surface gravity of Enceladus and  $\Delta H = 11$  km is the difference in ice thickness between the equator and the north pole.

The lateral salinity flux is given by the product of  $\Psi$  and a salinity contrast  $\Delta S$  and balances the salinity tendency due to freezing and melting yielding an equation for  $\Delta S$  thus (see a detailed derivation in *Marshall & Radko 2003*<sup>42</sup>):

$$\frac{\Psi \Delta S}{\pi a^2} = \rho_0 S_0 \Delta q \quad (4)$$

Here,  $\Delta q$ , the difference in the freezing rate between equator and pole, is chosen to be 4 km/Myr based on Fig.1b.  $a = 250$  km is the radius of Enceladus, and  $S_0$  is the mean salinity.

Combining Eq (2), Eq (3) and Eq (4), we can solve for  $\Delta S$  and  $\Psi$ . The only tunable parameter here is  $A$  which controls the strength of the overturning circulation and can be adjusted to yield that obtained in our ocean model. With  $A$  set to  $4.5 \times 10^{13}$  kg/s, we obtain the solutions shown by the empty circles in Fig.3 (the size of the circle reflect the amplitude of  $\Psi$ ), and compares well with the ocean model solutions. In particular, it captures the  $\beta_S \Delta S$  bulge and the weakening of  $\Psi$

---

<sup>4</sup>Ocean temperature at the water-ice interface is relaxed tightly toward the local freezing point, which varies by around 0.1K across latitude. Reducing the meridional temperature contrast by only 10% (ocean temperature deviates  $\delta T = 0.01$ K from the freezing point) would induce a heat flux of  $\gamma_T C_p \rho_0 \delta T = 400$  mW/m<sup>2</sup> ( $\gamma_T = 10^{-5}$  m/s is the water-ice exchange coefficient for temperature,  $C_p = 4000$  J/kg/K is the heat capacity of water and  $\rho_0$  is the reference water density given in Eq.8), which is unacceptably large.



at intermediate values of  $S_0$ . Furthermore, analogously to Eq (4), the meridional heat transport can be inferred from

$$\mathcal{H}_{\text{ocn}} = \frac{C_p \Psi \Delta T}{4\pi a^2}. \quad (5)$$

This is shown as a function of salinity and equator-to-pole thickness variations in Fig. 5a. In order to maintain the large thickness variation of the Enceladus ice shell (the likely/unlikely parameter regime is shaded in white/red) <sup>26–30</sup>, without introducing large discrepancies in the heat budget (i.e., water-ice heat exchange below the heat conduction rate of 50 mW/m<sup>2</sup>), an ocean salinity around 7–22 psu (marked by two vertical blue dashed lines) is required.

Our ocean simulation is of rather coarse resolution and somewhat diffusive due to limits of computational resource. But we can use our conceptual model to explore the circulation and transport of a less viscous ocean. The results for a 10 times larger  $A$  are shown by the empty diamonds in Fig.3.  $\Psi$  becomes roughly 10 times larger (notice the different size scales). The resultant rapid turnover time homogenises salinity gradients shifting all points closer to the  $\Delta S = 0$  limit. As a result, the transition from an  $\alpha$  ocean to a  $\beta$  ocean occurs around  $S_0 = 20$  psu: this is the optimum among all salinities required to sustain the observed ice geometry. With an even more vigorous overturning the transition approaches 22 psu, beyond which the anomalous expansion property of water disappears.

Another uncertainty of our model of freezing lies in the assumed ice rheology, which sets the melting rates and hence salinity gradients found just beneath the ice. Here we assumed that the melting point ice viscosity to be  $10^{14}$  Pa·s, an intermediate choice between an estimated lower

bound  $10^{13}$  Pa·s and an upper bound  $10^{15}$  Pa·s<sup>34</sup>. If the ice viscosity is, in fact, lower than assumed here, the ice flow and hence salinity exchange between water and ice would increase, and so would the salinity gradients within the ocean which are constrained at the surface. This results in an upward shift of the curves in Fig.3 and, as a result, the transition between the  $\beta$  and  $\alpha$  ocean will occur at lower salinities. The opposite is true if the ice is less mobile. To further constrain the problem requires a better understanding of ice rheology, perhaps anchored in laboratory experiments. Despite the uncertainties in ice rheology and ocean dynamics, our calculations suggest that Enceladus' ocean salinity is likely to be below 22 psu, the point at which the thermal expansion coefficient changes sign, as long as the equator is saltier and colder than the poles.

To conclude, we find that ocean dynamics on Enceladus strongly depends on its salinity and this in turn leads to a strong coupling with spatial variations in ice shell thickness. If the ocean is fresh, sinking occurs at the poles driven by the meridional temperature gradient; if the ocean is salty, sinking occurs at the equator driven by the salinity gradient. In both limits (very salty and very fresh), heat is converged equatorward (downgradient) by the overturning circulation, unlike previously proposed<sup>29</sup>. This is because the freezing point of water at the poles is higher than that at the equator and the magnitude of heat convergence is too large to be lost to space by heat conduction. As a result, ice geometry will be flattened. Only when salinity is in the mid-range and most of the heat production happens in the ice shell, can the temperature and salinity-driven overturning circulation cancel one-another, so that the equatorward heat transport is weak enough to be balanced by the polar-amplified heat production within the ice shell, and the observed ice thickness variations can be remained. Such cancellation is only possible near some specific tran-

sitional salinities lower than 22 psu, since equatorial waters are likely to be saltier and colder than polar waters as demanded by the poleward thinning ice geometry, Fig.1b). This transitional salinity separates the alpha ocean regime, featuring polar downwelling and equatorial upwelling (Fig.2 first column), and the beta ocean regime, featuring the opposite (Fig.2 third column). Because the relative height of buoyancy source and sink has different signs in an alpha ocean and a beta ocean, the ocean circulation develops much faster in the alpha ocean side as salinity deviates from the transitional salinity, making it more unlikely to have a salinity lower than the transitional than higher (Fig.4c). Having said that, salinity above 30 psu can lead to significant discrepancies in heat budget and thus seems implausible. As discussed in the introduction, such lower salinities are consistent with other observational estimates as well as predictions from chemical equilibrium between the rocky core and the ocean <sup>5</sup>. The circulation and hence heat transport are not sensitive to the partition of heat generation between the ice shell and the silicate core, but the overall heat budget is better closed if heat is mostly produced in the shell.

Insights from this study may also have implications for other icy moons. Europa is believed to have very high salinity ( $> 50$  psu, unfeasible parameter regime is shaded in red in Fig.5b) suggested by the strong magnetic induction field measured by the Galileo mission <sup>31</sup> (See *Khurana et al. 2009*<sup>43</sup>, *Vance et al. 2020* <sup>14</sup> for more discussion of uncertainties and possible ocean compositions). At such a high salinity, the ice pump mechanism and associated dynamics (as discussed above) would remove any fluctuations in the ice shell thickness, leaving a relatively flat ice sheet.

---

<sup>5</sup>Even when accounting for freezing of 21 km ice shell with zero salinity, a 22 psu present ocean salinity requires an initial ocean salinity of 13 psu which is consistent with geochemical estimates<sup>15,24,25</sup>

Applying our simplified model to Europa in Fig.5b, the predicted water-ice heat exchange becomes unphysically large (marked by the thick contour) when the equator-to-pole thickness variation is beyond 20% (marked by two horizontal blue dashed lines). This is consistent with the observation that the mean ice thickness is less 15 km (best match at 4 km) <sup>31,44</sup> and that no fissures such as the “tiger stripes” of Enceladus have been found. For icy moons with thicker ice shells, such as Dione, Titan, Ganymede, Callisto, the high pressure under the ice shell would remove the anomalous expansion for all salinities, making it impossible for the alpha and beta effects to cancel one another; meanwhile, the ice flow becomes very efficient, as it is proportional to the ice thickness cubed. Both of these processes suggest to us that icy ocean worlds with thick ice shells are likely to have small spatial shell thickness variation, consistent with shell thickness reconstruction based on gravity and shape measurements <sup>45–48</sup>. With future space missions (e.g., Europa Clipper), we expect that better observations of gravity, topography, and induced magnetic fields for icy moons will provide stronger constraints on ocean salinity and ice shell structure.

## **Methods**

### **Ocean General Circulation Model description.**

Our simulations are carried out using the state-of-the-art Massachusetts Institute of Technology OGCM (MITgcm <sup>32,33</sup>). The model integrates the non-hydrostatic primitive equations for an incompressible fluid in height coordinates including a full treatment of the Coriolis force in a deep fluid. In particular it can capture the dynamics of convection in the presence of planetary rotation which has a projection on to the local horizontal. These components are typically ignored when

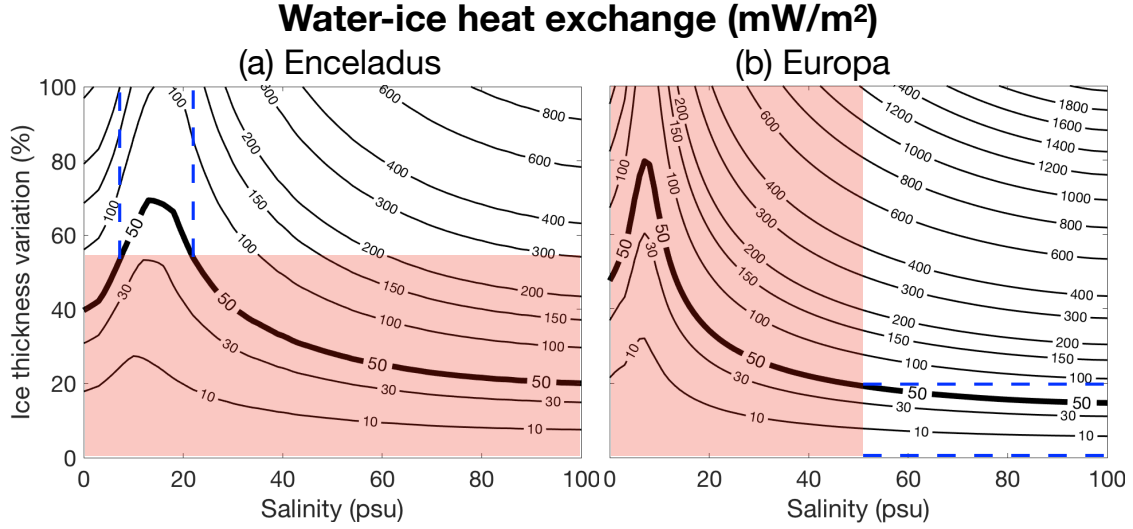


Figure 5: Application to other icy moons. The water-ice heat exchange equatorial predicted by the conceptual model (Eq.5) as a function of salinity and equator-to-pole percentage ice thickness variation (the equatorial ice thickness minus the polar ice thickness divided by the mean), assuming the variation has a degree-2 poleward-thinning structure. The two panels show for Enceladus, Europa ( $a = 1561$  km,  $g = 1.315$  m/s<sup>2</sup>, surface temperature  $T_s = 110$ K, mean ice thickness  $H = 15$  km<sup>31</sup>, mean ocean depth  $D = 85$  km), respectively. We highlight the 50 mW/m<sup>2</sup> contour using a thicker curve, as that is the maximum amount of heat can be lost by heat conduction through the equatorial ice shell. The Enceladus ice shell is expected to have large thickness variations<sup>26–30</sup>, and the Europa salinity is estimated to be higher than 50 psu<sup>31</sup>. The physically unlikely parameter regimes suggested by these observations are masked by red shadows, and plausible salinities for Enceladus and plausible ice thickness variations for Europa are enclosed by blue dashed lines.

simulating Earth’s ocean because of its small aspect ratio (the ratio between depth and horizontal scale of the ocean basin), but is crucial for Enceladus’s ocean, whose aspect ratio is instead order  $40\text{km}/252\text{km} \sim 0.16$  and so not small. The size of each grid cell shrinks with depth due to spherical geometry and is accounted for by switching on the “deepAtmosphere” option of MITgcm. Since the depth of Enceladus’s ocean is comparable to its radius, the variation of gravity with depth is significant. The vertical profile of gravity in the ocean and ice shell is given by, assuming a bulk density of  $\rho_{\text{out}} = 1000 \text{ kg/m}^3$ :

$$g(z) = \frac{G [M - (4\pi/3)\rho_{\text{out}}(a^3 - (a - z)^3)]}{(a - z)^2}. \quad (6)$$

In the above equation,  $G = 6.67 \times 10^{-11} \text{ N/m}^2/\text{kg}^2$  is the gravitational constant and  $M = 1.08 \times 10^{20} \text{ kg}$  and  $a = 252 \text{ km}$  are the mass and radius of Enceladus.

Since it takes several tens of thousands of years for our solutions to reach equilibrium, we employ a moderate resolution of 2 degree (8.7 km) and run the model in a 2D, zonal-average configuration whilst retaining full treatment of Coriolis terms. By doing so, the zonal variations are omitted. In fact, they are indeed negligible when the ocean is forced from above (as here), in accord with the “heat-from-above” scenario in *Kang et al. 2020*<sup>20</sup>. In the vertical direction, the 60 km ocean-ice layer is separated into 30 layers, each of which is 2 km deep. The ocean is encased by an ice shell with meridionally-varying thickness using MITgcm’s “shelfice” and ice “boundary layer” module<sup>49</sup>. We set the ice thickness  $H$  using the zonal average of the thickness map given by *Hemingway & Mittal 2019*<sup>30</sup>, as shown by the solid curve in Fig.1b, and assume hydrostacy (i.e., ice is floating freely on the water). We employ partial cells to better represent the ice topography: water is allowed to occupy a fraction of the height of a whole cell with an increment of 10%.

Due to the relatively coarse model resolution and use of a 2D configuration, convective processes are not resolved. We therefore adopt a much greater vertical diffusivity,  $1 \text{ m}^2/\text{s}$ , for temperature and salinity in regions that become statically unstable. Results are not found to be sensitive to this choice as long as the associated diffusive time scale  $D^2/\nu_{\text{conv}} \approx 0.5 \text{ yr}$  is much shorter than the advective time scale  $M_{\text{half}}/\Psi \approx 2000 \text{ yrs}$  ( $M_{\text{half}}$  is half of the total mass of the ocean and  $\Psi$  is the maximum meridional streamfunction in  $kg/s$ ).

We explore a wide range of background salinity from 4 psu to 40 psu, and adopt a linear equation of state (EOS which determines how density depends on temperature, salinity and pressure) to make the dynamics as transparent as possible. The dependence of potential density  $\rho$  on potential temperature  $\theta$  and salinity  $S$  is formulated as follows:

$$\rho(\theta, S) = \rho_0 - \alpha_T(\theta - \theta_0) + \beta_S(S - S_0) \quad (7)$$

$$\rho_0 = \rho(\theta_0, S_0). \quad (8)$$

Here,  $\rho_0$ ,  $\theta_0$  and  $S_0$  are the reference potential density, potential temperature and salinity.  $\alpha_T$  and  $\beta_S$ , the thermal expansion coefficient and the haline contraction coefficient, are set to the first derivative of density with respect to potential temperature and salinity at the reference point using the Gibbs Seawater Toolbox <sup>18</sup>. We carried out two test experiments (one with  $S_0 = 10 \text{ psu}$  and the other with  $S_0 = 20 \text{ psu}$ ) using the full “MDJWF” equation of state <sup>50</sup> and obtained almost identical results.

$S_0$  is prescribed to some value between 4 psu and 40 psu.  $\theta_0$  is set to be the freezing temperature at  $S_0$  and  $P_0 = 2.2 \times 10^6 \text{ Pa}$  (this is the pressure under a 20.8 km thick ice sheet on Enceladus).

Generally, freezing point  $T_f$  depends on local pressure  $P$  and salinity  $S$  following

$$T_f(S, P) = c_0 + b_0 P + a_0 S. \quad (9)$$

In the above equation, constants  $a_0 = -0.0575$  K/psu,  $b_0 = -7.61 \times 10^{-4}$  K/dbar and  $c_0 = 0.0901$  degC. The pressure  $P$  can be calculated using hydrostatic balance  $P = \rho_i g H$  ( $\rho_i = 917$  kg/m<sup>3</sup> is the density of the ice and  $H$  is the ice thickness).

Here we assume that the viscosity and diffusivity for temperature are the same as those for salinity, thus eliminating the possibility of double diffusive effects. We set the horizontal and vertical diffusivities to  $0.005$  m<sup>2</sup>/s, and the horizontal and vertical viscosities to  $50$  m<sup>2</sup>/s, the minimum required to control grid-scale noise. To smooth the solution near the water-ice interface we employ bi-harmonic hyperviscosity of  $3e9$  m<sup>4</sup>/s and a bi-harmonic hyperdiffusivity of  $5e7$  m<sup>4</sup>/s. It should be emphasised that away from boundary layers our solutions are close to geostrophic, hydrostatic and thermal wind balance.

We initialize the model from rest assuming zero salinity variations. The initial potential temperature at each latitude is set to be equal to the freezing point at the water-ice interface. The simulation is then launched for 10,000 years, by which time equilibrium has been reached.

**Boundary conditions.** Our ocean circulation model is forced by heat and salinity flux from the ice shell on the top as well as heat flux coming from below. On Enceladus, the heat loss to space by heat conduction  $\mathcal{H}_{\text{cond}}$  can be estimated using a 1D vertical heat conduction model,

$$\mathcal{H}_{\text{cond}} = \frac{\kappa_0}{H} \ln \left( \frac{T_f}{T_s} \right), \quad (10)$$



given the thickness of the ice  $H$  (solid curve in Fig.1b), the surface  $T_s$  and the ice temperature near the water-ice interface, which, by definition, is the local freezing point  $T_f$  (Eq. 9). We approximate the surface temperature  $T_s$  using radiative equilibrium based on the incoming solar radiation and obliquity ( $\delta = 27^\circ$ ) assuming an albedo of 0.81. The  $T_s$  profile is shown by the black solid curve in Fig.6.

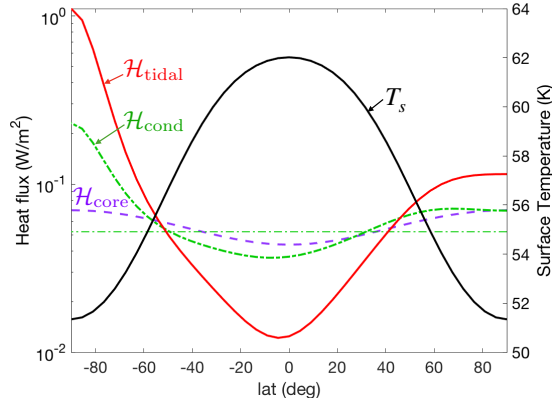


Figure 6: Meridional profiles of heat fluxes and surface temperature. Heat fluxes are plotted using coloured curves, with axis shown on the left. Conductive heat loss  $\mathcal{H}_{\text{cond}}$  (Eq. 10) is shown by a thick green dash-dotted line which, in the global average, is balanced by heat generation in the silicate core  $\mathcal{H}_{\text{core}}$  (purple dashed line, Eq. 11) and  $\mathcal{H}_{\text{tidal}}$  (red solid line, Eq. 15). All heat fluxes are normalized to have the same global mean value of  $\mathcal{H}_{\text{cond}}$ . The surface temperature  $T_s$  (black solid line, axis on the right) is set to be in radiative equilibrium with the solar radiation and is warmer at the equator.

This yields a heat loss rate  $\mathcal{H}_{\text{cond}}$  of 50 mW/m<sup>2</sup> which is primarily counterbalanced by tidal dissipation in the ice shell  $\mathcal{H}_{\text{tidal}}$  and the core  $\mathcal{H}_{\text{core}}$  (dissipation in the ocean plays a negligible role) <sup>51–54</sup>. For each assumed heat partition, we use the same heating profiles for  $\mathcal{H}_{\text{core}}$  and  $\mathcal{H}_{\text{tidal}}$  (see below). According to *Beuthe 2019*<sup>4</sup> and *Choblet et al. 2017*<sup>3</sup>, the core dissipation  $\mathcal{H}_{\text{core}}$  peaks

at the two poles. We obtain the meridional heat profile obtained using Eq.60 in *Beuthe 2019*<sup>4</sup> (with help from Beuthe),

$$\mathcal{H}_{\text{core}}(\phi) = \mathcal{H}_{\text{core}}(\phi) = \bar{\mathcal{H}}_{\text{core}} \cdot (1.08449 + 0.252257 \cos(2\phi) + 0.00599489 \cos(4\phi)), \quad (11)$$

where  $\phi$  denotes latitude and  $\bar{\mathcal{H}}_{\text{core}}$  is the global mean heat flux from the bottom. Since the global surface area shrinks going downward due to the spherical geometry, a factor of  $(a - H)^2 / (a - H - D)^2$  ( $H$  is ice thickness,  $D$  is ocean depth) needs to be considered when computing  $\bar{\mathcal{H}}_{\text{core}}$ . The above expression within the bracket is normalized for the globe, adjusted to take account of the fact that our model only covers 84S-84N. Using the above formula, the bottom heat flux is twice as strong over the poles than equator.

According to our previous work <sup>20</sup>, polar-amplified heating primarily in the ice shell is the most plausible explanation for thin ice over the poles. That said, assuming a heat partition of 20%-80% or even 100%-0% (core-shell) does not materially change our results. To illustrate, in the right hand column of Fig. 4, we present the heat transport in the extreme case where all the heating is assumed to be in the core.

At the upper (water-ice) boundary, we consider the response of the ocean to a prescribed ice freezing rate while ignoring the possible response of the ice to the water-ice heat/salinity exchange. The freezing/melting induces a salinity/fresh water flux into the ocean (we assume the ice salinity to be zero); meanwhile, the ocean temperature at the upper boundary is relaxed to the local freezing point  $T_f$  determined by the local salinity and pressure (Eq. 9).

$$\frac{dS_{\text{ocn-top}}}{dt} = \frac{qS_{\text{ocn-top}}}{\delta z} \quad (12)$$

$$\frac{dT_{\text{ocn-top}}}{dt} = \frac{1}{\delta z}(\gamma_T - q)(T_f - T_{\text{ocn-top}}) \quad (13)$$

Here,  $S_{\text{ocn-top}}$  and  $T_{\text{ocn-top}}$  denote the upper boundary salinity and temperature,  $\gamma_T = 10^{-5}$  m/s are the water-ice exchange coefficients for temperature and salinity,  $\delta z = 2$  km is the thickness of the water-ice “boundary layer” and  $q$  is the freezing rate in m/s (note that  $q$  is orders of magnitude smaller than  $\gamma_T$ ).

We prescribe  $q$  using the divergence of the ice flow, assuming the ice sheet geometry is in equilibrium. We use an upside-down land ice sheet model to calculate the downgradient ice flow following *Ashkenazy et al. 2018*<sup>36</sup>. The ice flows downgradient, driven by the pressure gradient induced by the spatial variation of the ice top surface, somewhat like a second order diffusive process. At the top, the ice flow speed is negligible because the upper part of the ice shell is cold and rigid and hence hard to move; at the bottom, the vertical shear of the ice flow speed vanishes, as required by the zero tangential stress there. This is the opposite to that assumed in the land ice sheet model. In rough outline, we calculate the ice flow using the expression below obtained through repeated vertical integration of the force balance equation (the primary balance is between the vertical flow shear and the pressure gradient force), using the aforementioned boundary conditions to arrive at the following formula for ice transport  $\mathcal{Q}$ ,

$$\mathcal{Q}(\phi) = \mathcal{Q}_0 H^3 (\partial_\phi H / a) \quad (14)$$

$$\mathcal{Q}_0 = \frac{2(\rho_0 - \rho_i)g}{\eta_{\text{melt}}(\rho_0/\rho_i) \log^3(T_f/T_s)} \int_{T_s}^{T_f} \int_{T_s}^{T(z)} \exp \left[ -\frac{E_a}{R_g T_f} \left( \frac{T_f}{T'} - 1 \right) \right] \log(T') \frac{dT'}{T'} \frac{dT}{T}.$$

Here,  $\phi$  denotes latitude,  $a = 252$  km and  $g = 0.113$  m/s<sup>2</sup> are the radius and surface gravity of Enceladus,  $T_s$  and  $T_f$  are the temperature at the ice surface and the water-ice interface (equal to

local freezing point, Eq. 9), and  $\rho_i = 917 \text{ kg/m}^3$  and  $\rho_0$  are the ice density and the reference water density (Eq. 7).  $E_a = 59.4 \text{ kJ/mol}$  is the activation energy for diffusion creep,  $R_g = 8.31 \text{ J/K/mol}$  is the gas constant and  $\eta_{\text{melt}}$  is the ice viscosity at the freezing point. The latter has considerable uncertainty ( $10^{13}$ - $10^{16} \text{ Pa}\cdot\text{s}$ )<sup>34</sup> but we choose to set  $\eta_{\text{melt}} = 10^{14} \text{ Pa}\cdot\text{s}$ . The dashed curve in Fig.1b shows the resultant freezing rate given our specification of  $H$ . Ice melts in high latitudes and forms in low latitudes at a rate of a few kilometers every million years: – see *Kang and Flierl 2020*<sup>39</sup> and *Ashkenazy et al. 2018*<sup>36</sup> for more details.

### **Brief summary of the tidal dissipation model.**

Enceladus’s ice shell is periodically deformed by tidal forcing and the resulting strains in the ice sheet produce heat. We follow *Beuthe 2019*<sup>4</sup> to calculate this dissipation rate. Instead of repeating the whole derivation, we only briefly summarize the procedure and present the final result. Unless otherwise stated, parameters are the same as assumed in *Kang & Flierl 2020*<sup>39</sup>.

Tidal dissipation consists of three components<sup>4</sup>: a membrane mode  $\mathcal{H}_{\text{tide}}^{\text{mem}}$  due to the extension/compression and tangential shearing of the ice membrane, a mixed mode  $\mathcal{H}_{\text{tide}}^{\text{mix}}$  due to vertical shifting, and a bending mode  $\mathcal{H}_{\text{tide}}^{\text{bend}}$  induced by the vertical variation of compression/stretching. Following *Beuthe 2019*<sup>4</sup>, we first assume the ice sheet to be completely flat. By solving the force balance equation, we obtain the auxiliary stress function  $F$ , which represents the horizontal displacements, and the vertical displacement  $w$ . The dissipation rate  $\mathcal{H}_{\text{tide}}^{\text{flat},x}$  (where  $x = \{\text{mem}, \text{mix}, \text{bend}\}$ ) can then be written as a quadratic form of  $F$  and  $w$ . In the calculation, the ice properties are derived assuming a globally-uniform surface temperature of 60K and a melting

viscosity of  $5 \times 10^{13}$  Pa·s.

Ice thickness variations are accounted for by multiplying the membrane mode dissipation  $\mathcal{H}_{\text{tide}}^{\text{flat,mem}}$ , by a factor that depends on ice thickness. This makes sense because this is the only mode which is amplified in thin ice regions (see *Beuthe 2019<sup>4</sup>*). This results in the expression:

$$\mathcal{H}_{\text{tide}} = (H/H_0)^{p_\alpha} \mathcal{H}_{\text{tide}}^{\text{flat,mem}} + \mathcal{H}_{\text{tide}}^{\text{flat,mix}} + \mathcal{H}_{\text{tide}}^{\text{flat,bend}}, \quad (15)$$

where  $H$  is the prescribed thickness of the ice shell as a function of latitude and  $H_0$  is the global mean of  $H$ . Since thin ice regions deform more easily and produce more heat,  $p_\alpha$  is negative. Because more heat is produced in the ice shell, the overall ice temperature rises, which, in turn, further increases the mobility of the ice and leads to more heat production (the rheology feedback).

Using reasonable parameters for Enceladus,  $\mathcal{H}_{\text{tide}}$  turns out to be at least an order of magnitude smaller than the heat loss rate  $\mathcal{H}_{\text{cond}}$ . This is a universal flaw of present tidal dissipation models, and could be due to use of an over-simplified Maxwell rheology <sup>16,55</sup>. We therefore scale up  $\mathcal{H}_{\text{tide}}$  by a constant factor to obtain the desired magnitude. The tidal heating profile corresponding to  $p_\alpha = -1.5$  is the red solid curve plotted in Fig. 6. In Fig. 4b, we show the tidal heating profile for  $p_\alpha = -1$  and  $p_\alpha = -2$ .

## Data Availability

The data sets generated during and/or analysed during the current study are available from the corresponding author on reasonable request.

## Code Availability

The MITgcm model used in the current study is publicly available. The codes used to do the analysis are available from the corresponding author on reasonable request.

1. Postberg, F. *et al.* Sodium salts in e-ring ice grains from an ocean below the surface of enceladus. *Nature* **459**, 1098–1101 (2009).
2. Thomas, P. *et al.* Enceladus’s measured physical libration requires a global subsurface ocean. *Icarus* **264**, 37–47 (2016).
3. Choblet, G. *et al.* Powering prolonged hydrothermal activity inside Enceladus. *Nature Astronomy* **1**, 841–847 (2017).
4. Beuthe, M. Enceladus’s crust as a non-uniform thin shell: Ii tidal dissipation. *Icarus* **332**, 66 – 91 (2019).
5. Waite, J. H. *et al.* Cassini Ion and Neutral Mass Spectrometer: Enceladus Plume Composition and Structure. *Science* **311**, 1419–1422 (2006).
6. Hsu, H.-W. *et al.* Ongoing hydrothermal activities within enceladus. *Nature* **519**, 207–210 (2015).
7. Waite, J. H. *et al.* Cassini finds molecular hydrogen in the Enceladus plume: Evidence for hydrothermal processes. *Science* **356**, 155–159 (2017).

8. Postberg, F. *et al.* Macromolecular organic compounds from the depths of enceladus. *Nature* **558**, 564–568 (2018).
9. Taubner, R.-S. *et al.* Biological methane production under putative enceladus-like conditions. *Nature communications* **9**, 1–11 (2018).
10. Glein, C. R. & Waite, J. H. The Carbonate Geochemistry of Enceladus' Ocean. *Geophysical Research Letters* **47**, 591 (2020).
11. Hansen, C. J. *et al.* Enceladus' Water Vapor Plume. *Science* **311**, 1422–1425 (2006).
12. Howett, C. J. A., Spencer, J. R., Pearl, J. & Segura, M. High heat flow from Enceladus' south polar region measured using 10-600 cm<sup>-1</sup> Cassini/CIRS data. *Journal of Geophysical Research-Atmospheres* **116**, 189 (2011).
13. Spencer, J. R. *et al.* Enceladus Heat Flow from High Spatial Resolution Thermal Emission Observations. *European Planetary Science Congress* **8**, EPSC2013–840 (2013).
14. Vance, S. D. *et al.* Magnetic induction in convecting galilean oceans. *arXiv preprint arXiv:2002.01636* (2020).
15. Glein, C., Postberg, F. & Vance, S. The geochemistry of enceladus: Composition and controls. *Enceladus and the icy moons of Saturn* **39** (2018).
16. McCarthy, C. & Cooper, R. F. Tidal dissipation in creeping ice and the thermal evolution of Europa. *Earth and Planetary Science Letters* **443**, 185–194 (2016).

17. Tobie, G., Mocquet, A. & Sotin, C. Tidal dissipation within large icy satellites: Applications to europa and titan. *Icarus* **177**, 534–549 (2005).
18. McDougall, T. J. & Barker, P. M. Getting started with teos-10 and the gibbs seawater (gsw) oceanographic toolbox. *SCOR/IAPSO WG* **127**, 1–28 (2011).
19. Soderlund, K. M. Ocean Dynamics of Outer Solar System Satellites. *Geophysical Research Letters* **46**, 8700–8710 (2019).
20. Kang, W. *et al.* Differing enceladean ocean circulation and ice shell geometries driven by tidal heating in the ice versus the core. *arXiv preprint arXiv:2008.03764* (2020).
21. Zhu, P., Manucharyan, G. E., Thompson, A. F., Goodman, J. C. & Vance, S. D. The influence of meridional ice transport on europa’s ocean stratification and heat content. *Geophysical Research Letters* **44**, 5969–5977 (2017).
22. Spencer, J. *et al.* Plume origins and plumbing: from ocean to surface. In *Enceladus and the Icy Moons of Saturn*, 163–174 (University of Arizona Press Tucson, 2018).
23. Ingersoll, A. P. & Nakajima, M. Controlled boiling on enceladus. 2. model of the liquid-filled cracks. *Icarus* **272**, 319–326 (2016).
24. Zolotov, M. Y. An oceanic composition on early and today’s Enceladus. *Geophysical Research Letters* **34** (2007).
25. Zolotov, M. Y. & Postberg, F. Can nano-phase silica originate from chondritic fluids? the application to enceladus’ sio<sub>2</sub> particles. *LPI* 2496 (2014).



26. Iess, L. *et al.* The Gravity Field and Interior Structure of Enceladus. *Science* **344**, 78–80 (2014).
27. Beuthe, M., Rivoldini, A. & Trinh, A. Enceladus’s and Dione’s floating ice shells supported by minimum stress isostasy. *Geophysical Research Letters* **43**, 10,088–10,096 (2016).
28. Tajeddine, R. *et al.* True polar wander of Enceladus from topographic data. *Icarus* **295**, 46–60 (2017).
29. Čadek, O. *et al.* Long-term stability of enceladus’ uneven ice shell. *Icarus* **319**, 476–484 (2019).
30. Hemingway, D. J. & Mittal, T. Enceladus’s ice shell structure as a window on internal heat production. *Icarus* **332**, 111–131 (2019).
31. Hand, K. & Chyba, C. Empirical constraints on the salinity of the euroman ocean and implications for a thin ice shell. *Icarus* **189**, 424–438 (2007).
32. MITgcm-group. MITgcm User Manual. Online documentation, MIT/EAPS, Cambridge, MA 02139, USA (2010).  
[http://mitgcm.org/public/r2\\_manual/latest/online\\_documents/manual.html](http://mitgcm.org/public/r2_manual/latest/online_documents/manual.html).
33. Marshall, J., Adcroft, A., Hill, C., Perelman, L. & Heisey, C. A finite-volume, incompressible Navier Stokes model for studies of the ocean on parallel computers. *J. Geophys. Res.* **102**, 5,753–5,766 (1997).

34. Tobie, G., Choblet, G. & Sotin, C. Tidally heated convection: Constraints on Europa's ice shell thickness. *J. Geophys. Res - Atmospheres* **108**, 219 (2003).
35. Barr, A. C. & Showman, A. P. Heat transfer in europa's icy shell. In *Europa*, 405–430 (Univ. Arizona Press, 2009).
36. Ashkenazy, Y., Sayag, R. & Tziperman, E. Dynamics of the global meridional ice flow of Europa's icy shell. *Nature Astronomy* **2**, 43–49 (2018).
37. Lewis, E. & Perkin, R. Ice pumps and their rates. *J. Geophys. Res* **91**, 756–11 (1986).
38. Czaja, A. & Marshall, J. The partitioning of poleward heat transport between the atmosphere and ocean. *Journal of the atmospheric sciences* **63**, 1498–1511 (2006).
39. Kang, W. & Flierl, G. Spontaneous formation of geysers at only one pole on enceladus's ice shell. *PNAS* **117**, 14764–14768 (2020).
40. Sandström, J. W. *Dynamische versuche mit meerwasser* (Ann. Hydrogr. Mar. Meteorol., 1908).
41. Jeffreys, H. On fluid motions produced by differences of temperature and humidity. *Quarterly Journal of the Royal Meteorological Society* **51**, 347–356 (1925).
42. Marshall, J. & Radko, T. Residual-mean solutions for the antarctic circumpolar current and its associated overturning circulation. *J. Phys. Oceanogr.* **33**, 2341–2354 (2003).

43. Khurana, K. K., Kivelson, M. G., Hand, K. P. & Russell, C. T. Electromagnetic induction from europa's ocean and the deep interior. *Robert. T. Pappalardo, William. B. McKinnon, and K. Khurana, Editors. Europa, University of Arizona Press, Tucson* 572–586 (2009).
44. Park, R. S. *et al.* Improved detection of tides at Europa with radiometric and optical tracking during flybys. *Planetary and Space Science* **112**, 10–14 (2015).
45. Zannoni, M., Hemingway, D., Casajus, L. G. & Tortora, P. The gravity field and interior structure of dione. *Icarus* 113713 (2020).
46. Durante, D., Hemingway, D., Racioppa, P., Iess, L. & Stevenson, D. Titan's gravity field and interior structure after cassini. *Icarus* **326**, 123–132 (2019).
47. Nimmo, F. & Bills, B. Shell thickness variations and the long-wavelength topography of titan. *Icarus* **208**, 896–904 (2010).
48. Vance, S. D. *et al.* Magnetic induction in convecting galilean oceans. *arXiv preprint arXiv:2002.01636* (2020).
49. Losch, M. Modeling ice shelf cavities in a z coordinate ocean general circulation model. *J. Geophys. Res.* **113**, 10.1029/2007JC004368 (2008).
50. McDougall, T. J., Jackett, D. R., Wright, D. G. & Feistel, R. Accurate and Computationally Efficient Algorithms for Potential Temperature and Density of Seawater. *Journal of Atmospheric and Oceanic Technology* **20**, 730–741 (2003).

51. Chen, E M A & Nimmo, F. Obliquity tides do not significantly heat Enceladus. *Icarus* **214**, 779–781 (2011).
52. Beuthe, M. Crustal control of dissipative ocean tides in Enceladus and other icy moons. *Icarus* **280**, 278–299 (2016).
53. Hay, H. C. F. C. & Matsuyama, I. Nonlinear tidal dissipation in the subsurface oceans of Enceladus and other icy satellites. *Icarus* **319**, 68–85 (2019).
54. Requier, J., Trinh, A., Triana, S. & Dehant, V. Internal energy dissipation in enceladus’s subsurface ocean from tides and libration and the role of inertial waves. *Journal of Geophysical Research: Planets* **124**, 2198–2212 (2019).
55. Renaud, J. P. & Henning, W. G. Increased Tidal Dissipation Using Advanced Rheological Models: Implications for Io and Tidally Active Exoplanets. *Astrophysical Journal* **857**, 98 (2018).

**Acknowledgements** This work is carried out in the Department of Earth, Atmospheric and Planetary Science (EAPS) in MIT. WK and TM acknowledges support as a Lorenz/Crosby Fellow supported by endowed funds in EAPS. SB, JC and JM acknowledge part-support from NASA Astrobiology Grant 80NSSC19K1427 “Exploring Ocean Worlds”. We thank Mikael Beuthe and Malte Jansen for help and discussions.

**Correspondence.** Correspondence and requests for materials should be addressed to Wanying Kang (email: wanying@mit.edu).